PAN

Opto-Electronics Review

journal homepage: https://journals.pan.pl/opelre

Long wavelength type-II superlattice barrier infrared detector for CubeSat hyperspectral thermal imager

Sir B. Rafol[1], Sarath D. Gunapala[1], David Z. Ting[1], Alexander Soibel[1], Arezou Khoshakhlagh[1], Sam A. Keo[1], Brian J. Pepper[1], Cory J. Hill[1], Yuki Maruyama[1], Anita M. Fisher[1], Ashok Sood[2], John Zeller[2], Robert Wright[3], Paul Lucey[3], Miguel Nunes[3], Luke Flynn[3], Sachidananda Babu[4], Parminder Ghuman[4]

[1] Center for Infrared Photodetectors, Jet Propulsion Laboratory, California Institute of Technology Pasadena, California, USA
[2] Magnolia Optical Technologies, Inc, Albany New York 12203, USA
[3] Hawai'i Institute of Geophysics and Planetology, University of Hawai'i at Manoa, Honolulu, Hawaii, USA
[4] NASA Earth Science Technology Office Greenbelt, Maryland, USA

Article info

Article history:
Received 03 Nov. 2022
Received in revised form 21 Dec. 2022
Accepted 30 Dec 2022
Available on-line 24 Feb. 2023

Keywords:
Type-II superlattice; focal plane array; infrared detector; quantum efficiency; noise equivalent difference temperature; dark current density; anti-reflective coating.

Abstract

The hyperspectral thermal imaging instrument for technology demonstration funded by NASA's Earth Science Technology Office under the In-Space Validation of Earth Science Technologies program requires focal plane array with reasonably good performance at a low cost. The instrument is designed to fit in a 6U CubeSat platform for a low-Earth orbit. It will collect data on hydrological parameters and Earth surface temperature for agricultural remote sensing. The long wavelength infrared type-II strain layer superlattices barrier infrared detector focal plane array is chosen for this mission. With the driving requirement dictated by the power consumption of the cryocooler and signal-noise-ratio, cut-off wavelengths and dark current are utilized to model instrument operating temperature. Many focal plane arrays are fabricated and characterised, and the best performing focal plane array that fulfils the requirements is selected. The spectral band, dark current and 8–9.4 μm pass band quantum efficiency of the candidate focal plane array are: 8–10.7 μm, $2.1 \cdot 10^{-5}$ A/cm^2, and 47%, respectively. The corresponding noise equivalent difference temperature and operability are 30 mK and 99.7%, respectively. Anti-reflective coating is deposited on the focal plane array surface to enhance the quantum efficiency and to reduce the interference pattern due to an absorption layer parallel surfaces cladding material.

1. Introduction

In high spatial and spectral resolution long wavelength infrared (LWIR) hyperspectral thermal imager (HyTI) applications, the focal plane array (FPA) is one of the major components that dictates the overall performance of the instrument. It is preferred that the FPA operates in detector noise-limited performance dominated by the signal source [1, 2]. The HyTI spectral range is within the 8–14 μm atmospheric transmission window ideal for a low-Earth orbit (LEO) deployment [3]. It also requires the FPA to have excellent uniformity, high operability, low dark current J_D and high quantum efficiency (QE) [4]. NASA's Earth Science Technology Office (ESTO) under the In-Space Validation of Earth Science Technologies (InVEST)-17 program is funding this hyperspectral thermal imager payload for the 6U LEO CubeSat platform. HyTI CubeSat instrument is a technology demonstration project that will monitor water resources and land surface temperature [4]. One of the goals of the instrument is to enable remote sensing of agricultural region. To maintain a high-resolution ground sampling distance, it requires a high frame rate operation of the HyTI instrument. The HyTI CubeSat instrument project is designed and developed by University of Hawaii – Hawaii Space Flight Laboratory (HSFL) and Jet Propulsion Laboratory (JPL) with the attempt to match Landsat instrument performance [5]. NASA JPL will deliver the FPA that is packaged inside a dewar. In close proximity to the surface of the FPA, there is a Fabry-Perot interferometer [4, 6]. In principle, an

*Corresponding author at: Sir.B.Rafol@jpl.nasa.gov

https://doi.org/10.24425/opelre.2023.144569
1896-3757/ Association of Polish Electrical Engineers (SEP) and Polish Academic of Sciences (PAS). Published by PAS

interferogram can be constructed for each point on the ground. Since the interferogram construction requires collection of many frames, the FPA and electronics are required to be very stable for the duration of the data collection.

There are several detector/FPA technologies with various performance ranges and costs. However, imaging from a high altitude above the Earth depends on low J_D and high QE, especially for a narrow spectral bandwidth demanded by the instrument. The competing LWIR detectors are mercury/cadmium/telluride (MCT), quantum well infrared photodetector (QWIP), and type-II strain layer superlattices (T2SLS) barrier infrared detector (BIRD) [7]. Uncooled LWIR detectors are not considered a contender because of their low QE and low speed. MCT is based on II-VI compound and has the highest performing QE material [8–10]. QWIP, on the other hand, has very high uniformity, but low QE [11]. Unfortunately, QWIP will not have the performance at high speed demanded by the high frame rate operation necessary to satisfy the ground sampling distance at a high orbital speed. LWIR T2SLS BIRD has matured considerably, and the predicted performance has improved. This BIRD detector design allows the unobstructed flow of photogenerated current but restricts the flow of dark current [9, 12]. The LWIR BIRD detector developed at JPL is an excellent candidate which satisfies many of the requirements of the LWIR detector for the HyTI instrument [4]. The QE is very reasonable for the high frame operation. In addition, its uniformity, operability, and temporal stability are excellent [13]. This will help in the performance of HyTI instrument. JPL NASA team will deliver a high performance FPA that will fulfil the requirements of the HyTI instrument.

Anti-reflective coating (AR-coating) is another important process that the FPA surface must endure to increase the QE and to reduce the Fabry-Perot effect due to the thin detector with reflecting surfaces [14]. Several candidate FPAs are coated with a thin anti-reflective material. The AR-coating technique is a novel approach based on nanostructure technologies [15]. The AR-coating performance is validated by using a sample FPA with half AR-coated region and the other half uncoated. The AR-coated FPA sample was tested and characterised. The QE and spectral measurement will undoubtedly show that the AR-coating does indeed improve QE.

2. Focal plane array requirement

Table 1 tabulates the FPA initial requirement. The read out integrated circuit (ROIC) is a Lockheed Martin SBF193 with a pixel pitch of 24 μm and an array format of 640 × 512. It operates in a p-on-n hole injection mode. The SBF193 ROIC is chosen because of its good linearity characteristics and maturity. The well depth and ROIC noise are shown in Table 1. The FPA fill factor is roughly ~84% due to a pixel delineation. There is about a 2 μm gap between the adjacent pixels wall. The gap also prevents the photocurrent generated carrier to transit to the nearest neighbour and, thus, it prevents electronic cross talk. The sidewalls are passivated to prevent performance degradation. The instrument spectral band is between 8 and 10.7 μm which is further subdivided into many narrowband spectral channels [4].

Table 1.
HyTI FPA parameter requirement.

FPA	Requirement (@ 68 K)
Detector pixel size (μm)	22 ± 0.5
Full width spectral range (μm)	8–10.7
Quantum efficiency no ARC @ 10.7 μm	> 0.20
Operability (no larger than 2×2 cluster @ centre)	> 0.99
Dark current density J_D (A/cm^2)	$\leq 2 \cdot 10^{-5}$
Well depth (e-)	$> 8 \cdot 10^6$
ROIC noise (e-)	< 600
Operating temperature (K)	≥ 68

3. Dark current, QE, and operating temperature

The HyTI CubeSat instrument is a very compact system (~6U, where U is a 10 cm cube) and, with various subsystems, requires power to operate. The power that is allocated to the Stirling cryocooler is very limited and, therefore, it is imperative to operate at higher temperature. Operating the cryocooler at a higher temperature reduces its power consumption and can extend the life of the cooler [16]. Although LWIR BIRD FPA operates at higher temperature already, LWIR FPA still has to be cooled considerably to reduce the dark noise generated by J_D especially for LWIR detector [9, 17]. Assuming that the dark noise and background noise are the dominant source of noise, a signal-to-noise ratio (SNR) equal to one can be estimated. The corresponding noise from SNR = 1 can be equated to a signal which can be compared to the performance model. The model uses the QE requirement, optical system, and operating temperature to derive a signal in which a noise equivalent difference temperature (NEΔT) is estimated for each spectral channel band of the HyTI instrument. However, it is usually required to have a higher SNR, typically in the 100 s or more. Knowing the dark current requirement and using a Rule 07, an estimate of the operating temperature can be calculated [18, 19]. Hence, by optimizing the J_D, QE and cut-off wavelength for a given optical system configuration, an upper limit of operating temperature can be estimated. This operating temperature also helps in estimating the power consumption of the cryocooler based on thermal load, parasitic load and the manufacturer published data. Since LWIR at a 50% cut-off wavelength is 10.7 μm, it requires cooling which consumes considerable power. JPL designed and developed a low-cost BIRD FPA with high operability and uniformity. The HyTI BIRD FPA will have high operating temperature and, therefore, it can save on power consumption. The extra power can be allocated to other subsystems such as digital processor, communication system, etc. The J_D, QE, and operating temperature were chosen to optimally operate the instrument at 68 K. However, a much better performing FPA will have the potential to raise the operating temperatures even higher.

If an operating temperature of 68 K is assumed, 20X Rule 07 dark current is roughly ~$2 \cdot 10^{-5}$ A/cm^2 at a 10.7 μm cut-off wavelength [18]. It is important to reduce the J_D because it contributes to noise, limits the ROIC dynamic

range, and requires more cooling. The 20X factor is based on the previous single element detector results and is an overly conservative value. However, it is possible that a much lower J_D can result, and this can consequently lead to a higher operating temperature. Another possibility that will raise the temperature of operation is if the QE increases by AR-coating. An increase in signal will result in a better SNR. AR-coating of the selected FPAs will be pursued in this program.

2.1. *Single element detector QE and dark current density*

Single element detectors are characterised by their spectral QE and J_D. If the performance is acceptable, the wafers are processed into detector array. This is a standard procedure that is followed as part of the FPA wafer screening process. Figure 1 depicts back illumination QE *vs*. wavelength of a single element detector at 66 K without AR-coating external deposition. The QE at 10.7 μm is approximately ~0.2 e^-/photon, which is close to the QE requirement. AR-coating deposition should improve the QE significantly. The J_D *vs*. temperature at 100 mV bias is shown in Fig. 2. The J_D ~$1.8 \cdot 10^{-5}$ A/cm^2 at 68 K and 100 mV bias is very close to the requirement. This wafer is processed to produce the FPA in a 640 × 512 format with a pixel pitch of 24 μm and a fill factor of 84% [13].

3. NEΔT, operability, QE, J_D, and AR-coating

Characterisation and testing of HyTI LWIR FPA requires a very stable cryocooled dewar which can cool down to a minimum of 60 K. Temperature stability means that a large thermal mass in the cold finger provides thermal inertia against temperature fluctuation [16]. The cryo-cooled test dewar utilized for this test has taken a long time to reach an operating temperature of 68 K due to the high thermal mass of the cold finger and the cold shield assembly. The FPA and temperature sensor were mounted and wire bonded onto a 100-pin leadless chip carrier (LCC). The temperature sensor on the LCC monitors the temperature of the FPA. Cryocooler controller uses a separate temperature sensor to control and stabilise the temperature in the cold finger. The FPA mounted on an LCC is installed onto the cold finger inside the cryocooled dewar with an f/7.8 cold aperture. A clamp assembly keeps a constant pressure between the LCC and the cold finger and an indium shim between the cold finger and the LCC is used to enhance the thermal contact. The two temperature sensors are in a very close proximity. Germanium window allows a 1–12 μm infrared band to pass through with >97 % transmission. Since the FPA dissipates about <55 mW of power at a 30 Hz frame rate, the temperature difference between the LCC and the cold finger temperature is negligible. This conclusion is supported by the calibration result of several temperature sensors against the cold finger temperature with and without power applied to the FPA. The cryocooler temperature controller was set to an operating temperature of 68 K. Since the ROIC analogue output voltage digitisation occurs outside the cryocooled dewar, the cabling between the FPA and the electronics was kept short, and the electronics is placed close to the dewar. This minimizes external noise pickup.

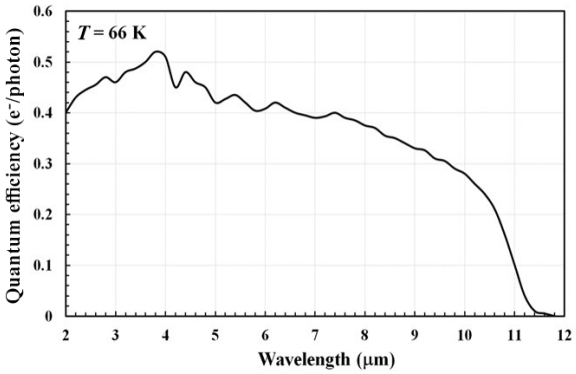

Fig. 1. QE *vs*. wavelength of a single detector element. Cut-off wavelength is ~10.5 μm.

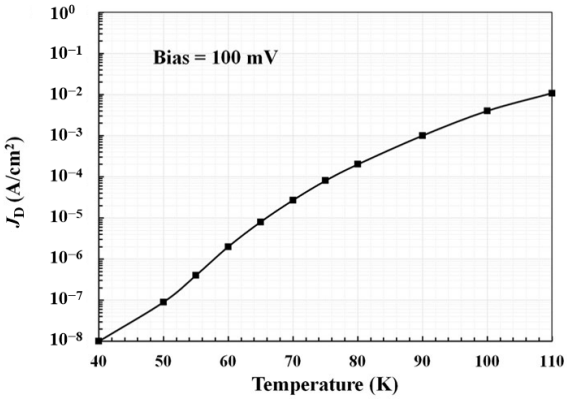

Fig. 2. J_D *vs*. temperature at 100 mV bias of a single detector element.

3.1. *FPA dark current density*

Measuring J_D of the FPA requires the cold shield and clamp assembly temperature to be the same temperature as the FPA. The aperture was blocked and allowed to reach equilibrium for at least three hours. This ensures that there is a very negligible background infrared radiation contribution from the cold shield and clamp assembly to the dark current measurement. Figure 3 shows the FPA J_D histogram at VDETCOM 5.2 V corresponding to the 100 mV detector bias. The mean and median are ~ $2.2 \cdot 10^{-5}$ A/cm^2 and ~$2.1 \cdot 10^{-5}$ A/cm^2, respectively at 68 K. This value is close to a single detector result (Fig. 2) and to the requirement. This low J_D value would not be possible without surface passivation. This is close to the 20X

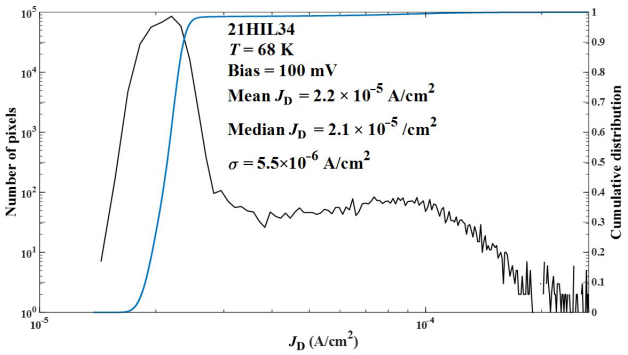

Fig. 3. Dark current density histogram of LWIR T2SLS BIRD FPA at a 100 mV bias and an operating temperature of 68 K.

Rule 07 requirement as predicted based on many results on LWIR samples. This is slightly higher than the requirement, but comparable to a single element result. At 68 K, the estimated photo current with a 4π field of view background flux from the cold shield and ROIC is low compared to J_D. The agreement between a single element and the mean J_D histogram is excellent. This shows that the passivation on the FPA is working as predicted. This FPA was thermally cycled more than 20X and the performance has not degraded.

3.2. *VDETCOM, bias determination and integration time*

To determine the operating bias at 68 K, the FPA stares at a flat black body at the constant temperature, usually at 300 K. The mean digital count output of the FPA *vs*. the VDETCOM bias traces a curve which provides important information on the VDETCOM bias voltage which is related to the detector bias. Figure 4 shows a plot of digitised output count *vs*. VDETCOM. It is apparent that the operating VDETCOM bias is close to the knee at about 5.15 V. A good voltage to bias the detectors is at about VDETCOM ~ 5.2 V. Biasing beyond the knee ensures that most pixels are biased in the plateau region in Fig. 4, since there is a distribution of the output count. Biasing below the knee will result in poor performance because a low debiasing can change the characteristics of the detector. Zero detector bias is at roughly VDETCOM ~5.1 V. The difference between 5.2 V and 5.1 V is about 100 mV which is the approximate detector bias and consistent with a single detector biasing. Higher VDETCOM values or higher bias do not improve performance. In fact, spatial nonuniformity ensues at higher VDETCOM. Most of the FPAs of similar design were biased at 100 mV. That is at VDETCOM ~ 5.2 V. This is close to the optimum operating bias. Once the VDETCOM (bias) was determined, the integration time was chosen to fill the charge well to about half to 2/3 of a full well when staring at the maximum temperature of the scene of interest. For this radiometric testing, a standard flat black body temperature is utilized. Temperature settings were 22 °C, 27 °C, and 32 °C. During the testing operation, VDETCOM and integration time are maintained at 5.2 V and ~1 msec, respectively using a standard fixed frame rate fixed of 27 Hz.

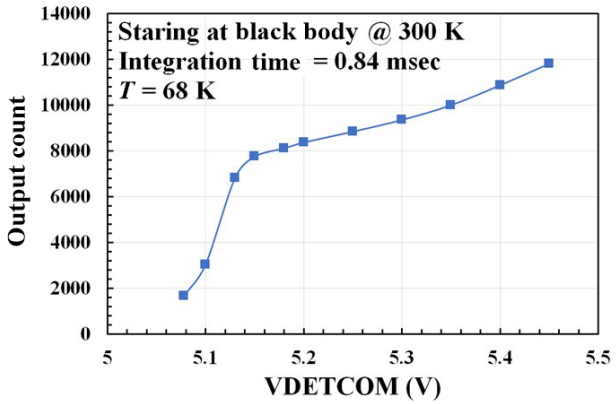

Fig. 4. FPA output count *vs*. VDETCOM for determining the proper bias.

3.3. *AR-coating and QE*

When infrared radiation falls from the vacuum side onto the FPA thin substrate, reflection and transmission of the radiation occur [14]. This is due to the optical property mismatch (refractive indices difference) at vacuum/substrate interface. Reflective radiation is considered a loss of signal. By AR-coating the FPA surface, this loss can be minimized considerably by suppressing reflection or maximizing transmission. Investigating the effect of AR-coating requires an experimental measurement of QE on the FPA. This is a direct measure of the immediate effect of AR-coating. The QE for the FPA can be estimated from the experimental data using the relationship

$$\mathrm{QE} = \frac{\Delta I_\mathrm{p}}{\Delta\Phi A_\mathrm{D} T_\mathrm{INT}}, \tag{1}$$

where ΔI_p is the measured photocurrent due to the differential photon flux $\Delta\Phi$ at two different black body temperatures, usually 295 K and 305 K. A_D is the detector area, and T_INT is the integration time. The photon flux $\Delta\Phi$ passing through a band pass filter is estimated using its full width half maximum (FWHM) spectral bandwidth as the limit of integration in the Planck's equation for photon flux [20]. FWHM of a band pass filter is usually provided by the manufacturer published data. To increase ΔI_p for a given detector at a constant $\Delta\Phi A_\mathrm{D} T_\mathrm{INT}$, the photon flux transmitted through the vacuum/substrate interface has to increase. Therefore, by minimizing the reflection of incident infrared radiation at the interface, ΔI_p will increase at a constant QE since there are more photons that can be absorbed.

As the QE is not 100% or not all photons are absorbed as they pass through the detector absorber (some transmitted radiation will be reflected from the lower electrical metal contact of the detector pixel). Thus, there are two surfaces retaining radiation with the top surface being partially reflecting. This will result in a Fabry-Perot Etalon-type optical interference due to multiple reflections. In other words, this results in a QE oscillation which is an undesirable consequence for the instrument [21]. AR-coating reduces the effect of the Fabry-Perot interference by decreasing the reflection at the vacuum/substrate interface and enhances the QE by increasing the transmitted radiation through the vacuum/substrate interface. The AR-coating material will reduce the reflective property at the interface of the two media with very different refractive indices. The AR-coating material is placed between vacuum and substrate for the FPA application.

Several FPAs were AR-coated utilizing a novel AR-coating technology described elsewhere [15]. Each AR-coated FPA was characterised and tested. To test this effect, half of the engineering grade FPA surface was AR-coated and the other half remained uncoated. This test will conclusively prove whether AR-coating will increase QE. Figure 5 shows the histogram distribution of the FPA that was half AR-coated and the other half uncoated. The presence of two distributions demonstrates that the AR-coated region QE is larger than the uncoated region QE. There is an increase of 12.1% in QE for an 8.075–9.4 μm band pass filter for the AR-coated region. This is a dramatic improvement. Note that the thickness of AR-coating and its

refraction index is related to the square root of the product of indices of air and GaSb substrate.

Figure 6 shows the QE histogram using a band pass filter from 8.075 to 9.4 μm for FPA 19HIL34 at 68 K and 5.2 V VDETCOM, which corresponds to 100 mV bias. This is an increase of 17%. This QE value was corrected for a transmission of the 8.075–9.4 μm band pass filter and the dewar window. Figure 7 shows the normalised response count *vs*. wavelength for the FPA before and after AR-coating. This measurement was made with a grating monochromator. Without AR-coating the response shows a larger amplitude of oscillation as a function of wavelength. This is due to the substrate/vacuum interface poor media matching. After AR-coating, the amplitude of oscillation is considerably reduced because the AR-coating material closely matched the two media. The vacuum/substrate interface media reflections are reduced internally and externally. This measurement can be related to spectral QE which can be obtained by normalising it with the reference and calibrated detector. Therefore, the presence of AR-coating on the FPA surface increases the QE and reduces the QE oscillation.

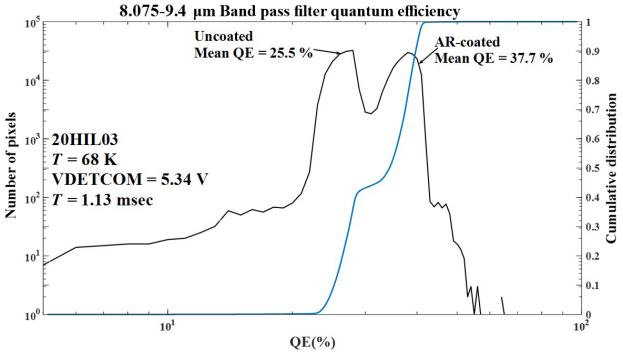

Fig. 5. QE histogram for the engineering grade FPA with the AR-coated half and the other half uncoated. The AR-coated region shows an increase in mean QE ~37.3%. The uncoated region shows a mean QE ~25.6%.

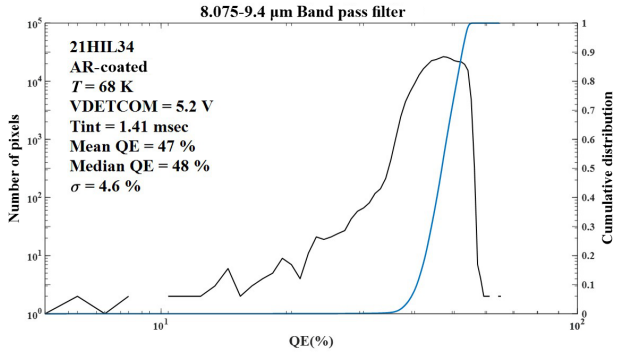

Fig. 6. QE histogram of a candidate HyTI T2SLS BIRD FPA with AR-coating.

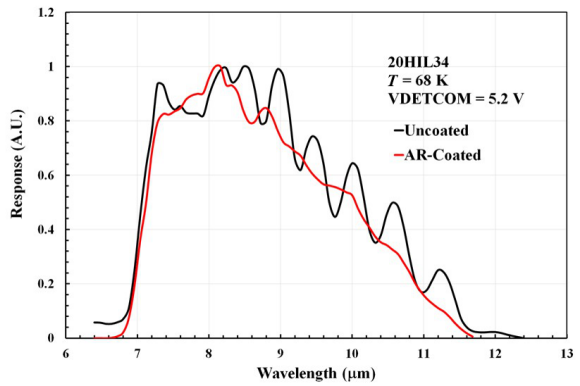

Fig. 7. Normalised spectral response of a candidate HyTI T2SLS BIRD FPA before and after AR-coating. The AR-coated plot shows less oscillatory fringes due to suppression of internal reflection.

3.4. *Noise equivalent difference temperature (NEΔT)*

NEΔT is of significant importance at a system level. It is assumed that the dominant noise source is the FPA. This is a measure of the thermal sensitivity to a small number of irradiances which can be detected by a low temperature difference. This can also be related to the minimum contrast temperature difference that will result in SNR = 1 [10, 22]. Hence, a lower temperature difference over a higher SNR will produce a lower value of NEΔT. This low NEΔT value will result in a more sensitive FPA. For experimental determination of NEΔT, 128 sequential frames are collected while the FPA is stared at 295 K, 300 K, and 305 K flat black body temperatures. The mean signal matrix is proportional to the mean difference between 305 K and 295 K responses. Taking the difference removes the offset on the data. The temporal noise σ is estimated at 300 K sequential data frames at a frame rate of 27 Hz. The NEΔT calculation is the following [22, 23]

$$\mathrm{NE\Delta T} = \frac{10 \cdot \sigma(300\ \mathrm{K})}{\mathrm{Mean}\,(305\ \mathrm{K}) - \mathrm{Mean}\,(295\ \mathrm{K})}, \qquad (2)$$

$$\text{where } \sigma^2 = \sum_{i=1}^{N} \frac{(\bar{x} - x_i)^2}{N}.$$

The NEΔT matrix is numerically evaluated. The Mean(295 K) and Mean(305 K) matrices are the mean evaluated at black body temperatures of $T_L = 295$ K and $T_H = 305$ K. The temporal noise is estimated at 300 K using 128 frames. Where $\bar{x}$ is the mean matrix of 128 frames taken at 300 K and x_i ($i = [1;128]$) is the individual frame. The σ as defined in the equation above shows that if few frames considerably deviate from the mean, it can significantly affect the root-mean-square (RMS) value. The experimentally estimated logarithmic plot of NEΔT histograms distributions at an operating temperature of 68 K, a bias of 100 mV, and an integration time of 840 μsec with a black body temperature of 300 K and a cold stop of f/7.8 is shown in Fig. 8. The mean NEΔT is 30 mK±3 mK at 68 K. This value of NEΔT implies good noise properties of detector and ROIC at short integration time T_{INT} ~0.84 msec. Also, it is noticeable that there is no significant long tail presence in the NEΔT histogram distribution. The NEΔT non-operable pixels are defined as those pixels which are open, shorted and >3× median NEΔT outliers. The full frame operability of this FPA is 99.7%. Bad pixel map shows the locations of pixels which are not electrically connected, shorted, and with NEΔT exceeding 3× median NEΔT value. Figure 9 is the bad pixel map image of the 512 × 320 central region of the FPA. Total number of bad pixels in the central 512 × 320 region is 405 pixels and there is no large cluster. The bad pixels

are the white dots in the image. Most of the bad pixels have a NEΔT value that exceeded 3× median. Note that the frame rate requirement for the instrument is quite high ~160 Hz. To achieve the high frame rate operation, a 512 V × 320 H windowing is implemented. For this FPA, the central region is obviously the best region to operate.

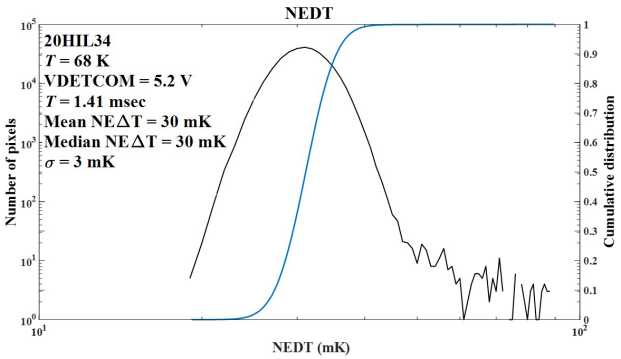

Fig. 8. NEΔT histogram distribution of the candidate HyTI T2SLS BIRD FPA after AR-coating.

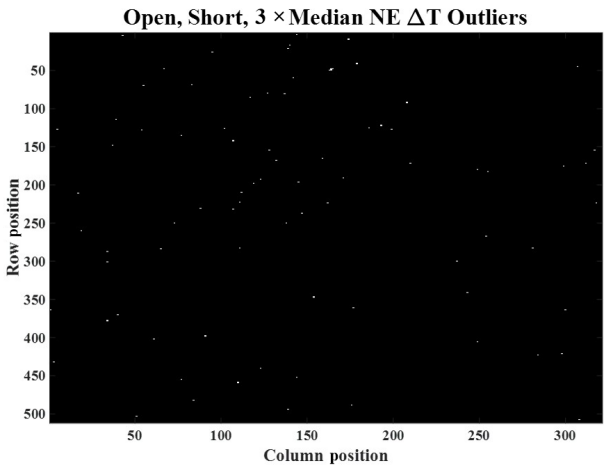

Fig. 9. Bad pixel map (white dot) of open, short, and 3X median outliers for the central 512 × 320 pixel, which has a total of 405 bad pixels.

3.5. Summary and conclusions

BIRD T2SLS device grown on a GaSb substrate was processed to produce test detectors and a 640 × 512 detector array format. The detector pixels are delineated and subsequently passivated to protect the pixel sidewalls from the formation of conductive surface layers. Single element devices from most wafers satisfy J_D and QE requirement. Better performing detector arrays are hybridised and epoxy-filled. The substrates were removed by diamond point turning, with about ≤30 µm of substrate material remaining. For some FPAs, the substrate was completely removed by chemical etching. The FPAs were characterised and tested, and relevant parameters such as J_D and QE were compared with results of a single element and the parameter agreement is very good. Most of the FPAs were characterised and tested with the extracted parameters compared to the requirement. Some FPAs were AR-coated to enhance the QE and to reduce the Fabry-Perot-type oscillation. Broadband mean and median NEΔT values ≤30 mK were obtained with an integration time of 0.84 msec and an operating temperature of 68 K. The NEΔT operability of most FPAs is > 99% with no cluster defects at the centre. The extracted band pass filter 8.075–9.4 µm mean QE for the best FPA ~47% after AR-coating, which also suppressed the Fabry-Perot oscillation interference. Several FPAs were thermally cycled for more than 30 times and no noticeable physical and electro-optical degradation was observed. These LWIR T2SLS BIRD FPA devices meet the requirements of the HyTI instrument program.

Acknowledgement

The authors thank the NASA Earth Science Technology Office and Jason Hyon, Eastwood Im, Nikzad Toomarian, and Harish Manohara of the Jet Propulsion Laboratory for encouragement and support. The research was carried out at the Jet Propulsion Laboratory, California Institute of Technology, under a contract with the National Aeronautics and Space Administration (80NM0018D0004). ©2022. All rights reserved. Government sponsorship acknowledged.

References

[1] Kinch, M. A. *Fundamentals of Infrared Detector Material*. (SPIE Press, Bellingham, Washington, 2007).

[2] Rogalski, A. *Infrared Detectors. Second Edition*. (CRC Press, Boca Raton, 2011).

[3] Willers, C. J. *Electro-optical System Analysis and Design. A Radiometry Perspective*. (SPIE Press, Bellington, Washington, 2013).

[4] Wright, R. *et al*. HYTI: High Spectral and Spatial Resolution Thermal Imaging from 6U CubeSat. in *34th Annual AIAA/USU, Conference on Small Satellites* (2021). https://digitalcommons.usu.edu/cgi/viewcontent.cgi?article=4618&context=smallsat

[5] Jhabvala, M., Choi, K,. S. Gunapala, M., Razeghi, M. & Sundaram, M. QWIPs, SLS, Landsat and international space station. *Proc. SPIE* **11288**, 1128801 (2020). https://ntrs.nasa.gov/api/citations/20190033892/downloads/20190033892.pdf

[6] Lucey, P. G., Horton, K., Williams, T. & Denevi, B. High-performance Sagnac interferometer using uncooled detectors for infrared hyperspectral applications. *Proc. SPIE* **6565**, 65650S (2007). https://doi.org/10.1117/12.718559

[7] Ting, D. Z. Progress in InAs/InAsSb superlattice barrier infrared detectors. *Proc. SPIE* **12107**, 121070O (2022). https://doi.org/10.1117/12.2618867

[8] Rogalski, A. HgCdTe infrared detectors: historical prospect. *Proc. SPIE* **4999**, *Quantum Sensing: Evolution and Revolution from Past to Future* (2003). https://doi.org/10.1117/12.479679

[9] Rogalski, A. InAs/GaSb type-II superlattice versus HgCdTe ternary alloys: future prospect. *Proc. SPIE* **10433**, 104330U (2017). https://doi.org/10.1117/12.2279572

[10] Kinch, M. A. *State-of-the-Art Infrared Detector Technology*. (SPIE Press, Bellingham, Washington, 2014).

[11] Gunapala, S. D. & Bandara, S. V. Quantum Well Infrared Photodetector (QWIP) Focal Plane Arrays. in *Semiconductors and Semimetals, Intersubband Transitions in Quantum Wells—Physics and Device Applications* (eds. Liu, H. C. Capasso, F.) Ch. 62, 197–280 (Academic Press, USA, 2000).

[12] Ting, D. Z. *et al*. Barrier infrared detector research at the Jet Propulsion Laboratory. *Proc. SPIE* **8511**, 851104 (2012). https://doi.org/10.1117/12.929810

[13] Gunapala, S. *et al*. Mid-wavelength and long-wavelength focal planes for smallsat applications. *Proc. SPIE* **12091**, 1209102 (2022). https://doi.org/10.1117/12.2619573

[14] Schallenberg, U. Design principle for broadband AR coatings *Proc. SPIE* **7101**, 710103 (2008). https://doi.org/10.1117/12.797708

[15] Sood, A. K. *et al*. Development of nanostructured antireflection coating technology of IR band for improved detector performance. Proc. SPIE **11858**, 185812 (2021). https://doi.org/10.1117/12.2598994

[16] Ross Jr, R. G. Refrigeration Systems for Achieving Cryogenic Temperatures. in *Low Temperature Materials and Mechanisms* (Ed. Bar-Cohen, J.) Ch. 6, 109–181 (CRC Press, Boca Raton, 2016).

[17] Plis, E. A. InAs/GaAs Type-II superlattice detectors. *Adv. Electron.* **2014**, 246769 (2014). https://doi.org/10.1155/2014/246769

[18] Tennant, W. E. "Rule 07" revisited: Still a good heuristic predictor of p/n HgCdTe photodiode performance*? J. Electron. Mater*. **39**, 1030–1035 (2010). https://doi.org/10.1007/s11664-010-1084-9

[19] Ting, D. Z. Progress in InAs/InAsSb superlattice barrier infrared detector. *Proc. SPIE* **12107**, 121070O (2022). https://doi.org/10.1117/12.2618867

[20] Palmer, J. M. & Grant, B. G. *The Art of Radiometry*. (SPIE Press Bellingham, Washington, 2010).

[21] Nguyen, B.-N. *et al*. High performance antimony type-II suplerlattice photodiodes on GaAs substrate. *Proc. SPIE* **7298**, 72981T (2009). https://doi.org/10.1117/12.818373

[22] Holst, G. C. Infrared Imaging System Testing. in *Electro-Optical Systems Design, Analysis and Testing* (ed. Dudzik, M. C.) Ch. 4 (SPIE Optical Engineering Press, Bellingham, 1993).

[23] Burke, M. J. & Wan, W. H. IR FPA sensor characterization and analysis using Matlab tm. *Proc. SPIE* **3377** (1998). https://doi.org/10.1117/12.319388